

# On the resonances of a rotating black hole analogue

Sam R. Dolan\*

*School of Mathematics, University of Southampton,  
Highfield, Southampton SO17 1BJ, United Kingdom*

Leandro A. Oliveira† and Luís C. B. Crispino‡

*Faculdade de Física, Universidade Federal do Pará, 66075-110, Belém, Pará, Brazil*

(Dated: June 7, 2022)

Under certain conditions, sound waves in a fluid may be governed by a Klein-Gordon equation on an ‘effective spacetime’ determined by the background flow properties. Here we study the ‘draining bathtub’ (DBT) system, a circulating, draining flow whose effective spacetime has key features in common with the rotating black hole (Kerr) spacetime. We investigate the spectrum of quasinormal (QN) mode and Regge pole resonances exhibited by the DBT, and we compare with the equivalent Kerr spectra. First, to demonstrate the ubiquity of ‘QN ringing’, we simulate the evolution of a perturbation in the time domain by applying a finite-difference method. Next, we solve the wave equation in the frequency domain, using the continued-fraction method to compute QN frequencies. We explore the geometric link between null geodesic orbits and QN frequencies, and apply an asymptotic method to provide an expansion of QN frequencies in inverse powers of mode number  $m$ . The same range of methods is then applied to study the (closely-related) Regge pole spectrum. Finally, we adapt complex angular momentum methods to explore the link between the Regge poles and oscillations in the absorption cross section.

PACS numbers: 04.70.-s, 04.30.Nk, 43.20.+g, 47.35.Rs, 11.55.Jy

## I. INTRODUCTION

Black holes – ‘trapped’ regions of spacetime – are a key element of Einstein’s theory of general relativity. Although perhaps once viewed as mathematical curiosities, astronomers have now compiled a range of compelling evidence for their existence. Black holes are a key ingredient in modern theories of galaxy formation, quasars, accretion disks, gamma ray bursts and supernovae [1–4]. Yet, even if black holes were nothing more than a theorist’s ‘thought experiment’, they would still have provoked the development of theoretical physics. In the 1970s, Hawking showed that quantum field theory in curved spacetime implies that black holes are not completely black: they must radiate thermally, with a negative heat capacity [5]. Furthermore, black holes seem to have a well-defined entropy, that scales with the horizon area. Hawking’s work has inspired myriad (and ongoing) attempts to consistently combine relativity and field theory in the strong field regime.

There is more to black holes than Hawking radiation. A key property of a black hole is that it bends and traps light. Light rays may orbit a black hole in the vicinity of a ‘photon sphere’ which lies somewhat outside the horizon (at  $r = 3r_h/2$  for the Schwarzschild BH, where  $r_h$  is the horizon radius) [6]. The existence of an unstable photon orbit gives rise to various interesting effects, such as the strong-field lensing of background light passing close to a

black hole. In particular, the photon orbit is intimately linked to characteristic ‘damped resonances’ that appear when waves interact with a black hole. Mathematically, damped resonances are manifest as poles in the scattering matrix  $S$  [1]. The poles occur at complex frequencies and at complex angular momenta, and the corresponding modes are known as quasinormal (QN) and Regge pole (RP) modes, respectively [2]. In this paper, we investigate QN and RP modes (and their physical consequences) in the setting of a simple rotating ‘black hole analogue’ [7].

It seems unlikely that we will ever study black holes directly in the laboratory. Yet, as Unruh [8] noted three decades ago, we may study analogues: artificial systems (in various media) which exhibit some key kinematic features of black holes [9]. For example, sound waves in fluid flows which are inviscid, irrotational, and barotropic are governed by the same wave equation as a scalar field in a curved space-time, namely [7]

$$\square\Phi = \frac{1}{\sqrt{|g|}}\partial_\mu\left(\sqrt{|g|}g^{\mu\nu}\partial_\nu\Phi\right) = 0, \quad (1)$$

where here  $g_{\mu\nu}$  is the *effective metric* (with inverse  $g^{\mu\nu}$  and determinant  $g$ ). Note that in this context,  $g_{\mu\nu}$  depends algebraically on the local properties of the fluid flow, and it does not (in general) represent a solution of the Einstein equations. Nevertheless, it is an intriguing prospect that, by studying sound waves on a background flow, one may understand better the propagation of fields on a curved spacetime. In recent years, a wide range of black hole analogues in various media have been proposed and, indeed, studied, in the laboratory [10–14]. A surge of recent experimental activity appears to be bear-

\*Electronic address: s.dolan@soton.ac.uk

†Electronic address: laoliveira@ufpa.br

‡Electronic address: crispino@ufpa.br

ing fruit, as evidenced by a recent claim of experimental observation of correlations related to Hawking radiation in a wave-tank [15].

One of the simplest analogue models is the so-called *draining bathtub* (or draining vortex), described in [7]: a two-dimensional circulating flow with a sink at the origin. In 2003, Schützhold and Unruh [16] described a possible experimental realization of the ‘bathtub’ idea, wherein gravity waves propagate in a flowing fluid in a shallow basin of varying height  $h(r)$ . Non-dispersive long-wavelength perturbations are governed by an effective geometry with line element  $ds^2 = g_{\mu\nu}dx^\mu dx^\nu$ , where

$$ds^2 = -c_s^2 d\tilde{t}^2 + \left(dr + \frac{Dd\tilde{t}}{r}\right)^2 + \left(r d\tilde{\phi} - \frac{C d\tilde{t}}{r}\right)^2. \quad (2)$$

Here the constants of circulation ( $C$ ) and draining ( $D$ ) [17] relate to the background flow velocity  $\mathbf{v}_0$  of the fluid, namely

$$\mathbf{v}_0 = -D\hat{r}/r + C\hat{\phi}/r. \quad (3)$$

The speed of sound in the fluid  $c_s$  is set by  $c_s^2 = a_g h_\infty$ , where  $a_g$  is the acceleration due to gravity and  $h_\infty$  is the height of the fluid far from the centre. The analogue event horizon (where the inward flow rate exceeds  $c_s$ ) lies at  $r_h = |D|/c_s$ , and the analogue ergosphere (where the flow becomes supersonic  $|\mathbf{v}_0| \geq c_s$ ) has a boundary at  $r_e = \sqrt{C^2 + D^2}/c_s$  [7]. Small perturbations  $\delta\mathbf{v}$  to the flow,  $\mathbf{v} = \mathbf{v}_0 + \delta\mathbf{v}$ , may be expressed in terms of a gradient of a potential  $\delta\mathbf{v} = -\nabla\Phi$ , and the potential field  $\Phi$  satisfies the Klein-Gordon equation (1) with effective metric (2). Henceforth we set the speed of sound equal to unity ( $c_s = 1$ ).

There are several key motivations for considering the draining bathtub (DBT). Firstly, as described above, the DBT may be realized in the laboratory. Secondly, the DBT provides a useful ‘toy model’ for the most astrophysically-relevant black hole, i.e. the Kerr solution. For example, both the DBT and the Kerr solution possess a horizon and an ergosphere, and can exhibit superradiance; but whereas the angular momentum of the (non-naked) Kerr black hole is constrained,  $J \leq M^2$ , the angular momentum of the DBT is (in principle) unbounded. This follows as a consequence of their differing symmetry: the DBT is cylindrically symmetric, whereas the Kerr solution is axially symmetric. A third reason is simplicity: the DBT is arguably the simplest asymptotically flat *rotating* spacetime that can be envisaged (see also the cosmic string [18]). It serves as a testing ground for developing calculation frameworks that can be extended to Kerr geometry.

Given such motivations, it is no surprise to find that the spectrum of quasinormal modes of the DBT has already received attention [19, 20] (although the Regge pole spectrum has not). We believe that a more comprehensive study is now justified, as we go several steps beyond existing work to show, for example, (i) how resonances arise in the time domain, as well as the frequency domain,

(ii) how resonances are closely related to the properties of the co- and counter-rotating null orbits, (iii) how complex angular momentum methods [21–25] can be applied to the compute absorption cross section [28] of the draining bathtub.

The remainder of this paper is structured as follows. In Sec. II we study perturbations and null geodesics in the DBT effective spacetime. In Sec. III we evolve generic perturbations in the time domain and identify the quasinormal mode ringing, applying the continued-fraction method to obtain the frequency spectrum of the DBT QN modes. We revisit the expansion method of Ref. [26, 27] and apply it to find the QN modes of the DBT. We validate the expansion method results by comparing them to the continued-fraction method ones. In Sec. IV we extend the asymptotic expansion method to find Regge poles, and introduce a numerical method to check the asymptotic expansion results. We also obtain the absorption cross section of the DBT [28] in terms of the Regge poles by using the complex angular momentum method [24, 25]. We conclude in Sec. V with some final remarks.

## II. THE DRAINING BATHTUB

The draining bathtub was briefly described in the previous section, and we address the reader to Ref. [7] for more details. In the lab-based coordinates  $\{\tilde{t}, r, \tilde{\phi}\}$ , the effective geometry is described by the line element (2). Following [19], it is convenient to introduce an alternative coordinate system  $\{t, r, \phi\}$  via  $dt = d\tilde{t} - Ddr/(rf)$ ,  $d\phi = d\tilde{\phi} - CDdr/(r^3 f)$ , with  $\phi(r \rightarrow \infty) \rightarrow \tilde{\phi}$  and

$$f(r) = 1 - D^2/r^2. \quad (4)$$

The line element (2) then takes the form

$$ds^2 = -f(r)dt^2 + f(r)^{-1}dr^2 + (rd\phi - Cdt/r)^2. \quad (5)$$

Henceforth we will work with these (non-lab based) coordinates exclusively.

### A. Perturbations

Small perturbations to the background flow,  $\delta\mathbf{v} = -\nabla\Phi$ , are governed by the Klein-Gordon equation (1) with line element (5). Let us now decompose  $\Phi$  in azimuthal modes, namely

$$\Phi(t, r, \phi) = \frac{1}{\sqrt{r}} \sum_{m=-\infty}^{\infty} \psi_m(t, r) e^{im\phi}. \quad (6)$$

Since  $\Phi$  is a real field, the symmetry relation  $\psi_m^* = \psi_{-m}$  follows. Inserting Eq. (6) into Eq. (1) leads to the wave equation

$$\left[ -\left( \frac{\partial}{\partial t} + \frac{iCm}{r^2} \right)^2 + \frac{\partial^2}{\partial r_*^2} - V_m(r) \right] \psi_m(t, r) = 0, \quad (7)$$

where

$$V_m(r) = f(r) \left[ \frac{m^2 - 1/4}{r^2} + \frac{5D^2}{4r^4} \right], \quad (8)$$

and the tortoise coordinate is defined by  $dr_* = f^{-1}dr$ , or, explicitly,

$$r_* = r + \frac{D}{2} \ln \left| \frac{r - D}{r + D} \right|. \quad (9)$$

A perturbation of compact support in the vicinity of the hole satisfies the boundary conditions

$$\lim_{r_* \rightarrow -\infty} [\partial_t + iCm/D^2 - \partial_{r_*}] \psi_m = 0, \quad (10)$$

$$\lim_{r_* \rightarrow +\infty} [\partial_t + \partial_{r_*}] \psi_m = 0. \quad (11)$$

### B. Geodesics

According to the eikonal approximation, very short-wavelength perturbations propagate along null geodesics of the effective spacetime (5), i.e.

$$\Phi \sim \exp(-ik_\mu x^\mu), \quad k_\mu k^\mu = 0, \quad k^\mu k_{\nu;\mu} = 0. \quad (12)$$

Hence, by investigating the null geodesics of the line element (5) we may understand high-frequency wave propagation. Let us consider a geodesic with tangent vector  $k^\mu = (\dot{t}, \dot{r}, \dot{\phi})$ , where the overdot denotes differentiation with respect to an affine parameter. Geodesics have two constants of motion, i.e., energy and angular momentum

$$\begin{aligned} E &= \left( 1 - \frac{D^2 + C^2}{r^2} \right) \dot{t} + C \dot{\phi}, \\ L &= -C \dot{t} + r^2 \dot{\phi}. \end{aligned}$$

For a null geodesic ( $k^\mu k_\mu = 0$ ) we may write the ‘energy equation’ as

$$\dot{r}^2 + V_{\text{geo}}(r) = E^2, \quad (13)$$

where

$$V_{\text{geo}}(r) = \left( 1 - \frac{D^2 + C^2}{r^2} \right) \frac{L^2}{r^2} + \frac{2CLE}{r^2}. \quad (14)$$

Let us consider a null geodesic impinging from infinity. Its ‘impact parameter’  $b$  may be defined as the perpendicular distance (measured at infinity) between the geodesic and a parallel line that passes through the origin,

$$b \equiv L/E + C.$$

Here  $b$  is defined as a displacement that may take either sign, allowing us to distinguish between co-rotating (+) and counter-rotating (−) geodesics. Now, if  $|b|$  is large, the geodesic will be scattered; if  $|b|$  is small, the geodesic will be absorbed (i.e. it will pass through the

horizon). Between these regimes is a ‘critical’ geodesic, which is neither scattered nor absorbed but instead ends in perpetual orbit at  $r = r_c^\pm$ . By solving simultaneous conditions  $V(r_c) = 0$  and  $dV/dr(r_c) = 0$  we find a pair of ‘critical’ geodesics given by

$$b_c^\pm = -C \pm 2\sqrt{D^2 + C^2}, \quad (15)$$

$$r_c^\pm = \left( \sqrt{D^2 + C^2} |b_c^\pm - C| \right)^{1/2}. \quad (16)$$

Note that  $b_c^-$  is defined to be negative.

For  $C > 0$ , geodesics with  $b > C$  ( $L > 0$ ) co-rotate with the system, whereas geodesics with  $b < C$  ( $L < 0$ ) counter-rotate with the acoustic hole. Hence it is natural to define  $l_c \equiv b - C$ , which is positive for co-rotating geodesics and negative for the counter-rotating ones, so that:

$$l_c^\pm \equiv b_c^\pm - C = -2C \pm 2\sqrt{D^2 + C^2}. \quad (17)$$

Trajectories of null geodesics impinging from spatial infinity upon a draining bathtub are illustrated in Ref. [28].

## III. QUASINORMAL MODE RESONANCES

With these preliminaries established, let us now turn our attention to quasinormal (QN) modes. We start in Sec. III A by demonstrating QN resonances in a perturbation encroaching upon a black hole, by evolving generic initial data in the time domain. In Sec. III B we recap the theory of QN modes as poles of the Green function in the frequency domain, and in Sec. III C we describe the symmetries of the spectrum and provide an exact solution for the non-resonant  $m = 0$  mode. Next, we apply two frequency-domain methods to determine the spectrum: the numerical method of [20], and the ‘geodesic expansion’ method of [26, 27]. We validate our results, compare with the Kerr spectrum, and give a geometric interpretation. Henceforth we set  $D = 1$  for convenience, unless otherwise stated.

### A. Quasinormal modes in the time domain

To study the phenomenon of QN mode ringing, let us consider the evolution of a small perturbation to the system. For concreteness, we take an initial condition of the form

$$\psi_m(t = 0, r_*) = \exp[-(r_* - r_{*0})^2/(2\sigma^2)], \quad (18)$$

$$\partial_t \psi_m(t = 0, r) = 0, \quad (19)$$

where  $r_{*0}$  and  $\sigma^2$  are arbitrary constants. Now, we simulate the evolution of this initial perturbation by applying finite-difference (FD) methods to the wave equation (7). There are many possible FD methods; we chose the ‘Method of Lines’ (described e.g. in Ref. [29] and Sec. 4.2 of Ref. [30]), using second-order differencing on

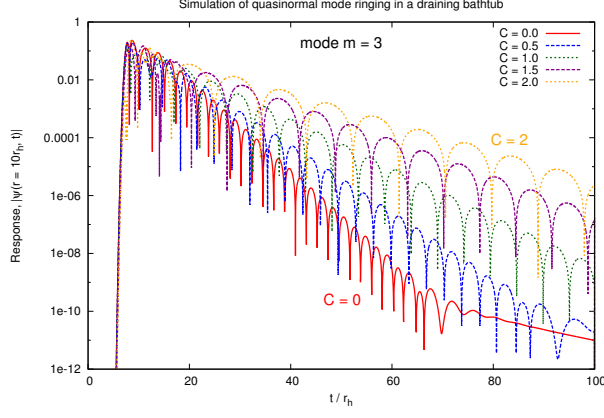


FIG. 1: Illustrating the ‘quasinormal ringing’ response as a function of time  $t$  of a draining bathtub to a generic initial perturbation. Here the value of  $\psi(t, r)$  at a fixed radius  $r = 10r_h$  is shown, for various values of the ‘circulation’  $C$  of the bathtub,  $C = 0 \dots 2$ . As the circulation rate increases, the ringing frequency and the damping rate decrease.

spatial slices and the fourth-order Runge-Kutta method to advance in time. This method was chosen primarily for its good stability properties: it is numerically stable provided that the time step  $\tau$  is small enough (typically we took  $\tau = h/2$  for our evolutions, where  $h$  is the spatial grid spacing). We made the spatial domain large enough in  $r_*$  that the ‘physical’ perturbation did not encounter the spatial boundaries during the simulation run.

Typical results are given in Fig. 1, which shows the response  $\psi_m(t, r)$  at fixed radius  $r = 10r_h$  as a function of time to an initial condition of the form (19). The logarithmic scale on the vertical axis shows that, at intermediate times, the response is apparently dominated by exponentially-damped ringing. This response is typical of systems with an unstable geodesic orbit (or equivalently a peak in the potential barrier). Ringing may be understood in terms of QN modes with characteristic complex frequencies  $\omega_{mn}^\pm$  which depends on parameters of the system ( $C$  and  $D$ ) rather than details of the initial perturbation.

The time-domain signal in Fig. 1 clearly shows the imprint of the least-damped QN mode. The damping rate and ringing frequency of this mode decreases as the circulation rate  $C$  increases; in Sec. III F we comment on this behavior. The ringing frequency increases with mode number  $m$ . Figure 2 shows that, at very late times, the signal is dominated by a power law decay,

$$\psi(t, r) \sim t^{-\eta},$$

where

$$\eta = \begin{cases} 2|m| + 1, & \partial_t \psi|_{t=0} \neq 0, \\ 2|m| + 2, & \partial_t \psi|_{t=0} = 0. \end{cases} \quad (20)$$

In other words, the decay is one power of  $t$  more rapid in the special case of time-symmetric initial data [such as

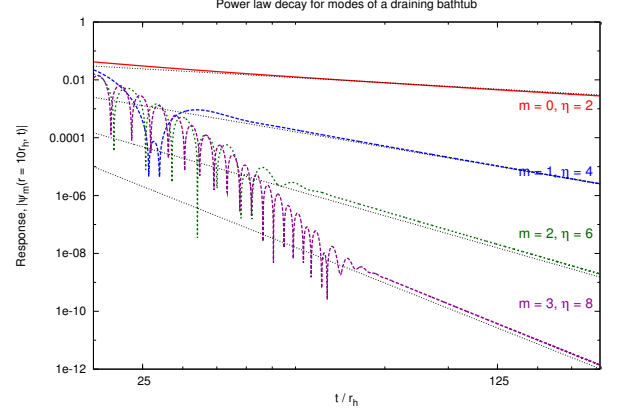


FIG. 2: Log-log plot illustrating ‘power law decay’ in modes  $m = 0 \dots 3$  for a generic perturbation of a draining bathtub. At late times, the perturbation decays as  $\psi \propto (t/r_h)^{-\eta}$ , where  $\eta = 2|m| + 1$  for generic initial data, and  $\eta = 2|m| + 2$  for time-symmetric initial data,  $\partial_t \psi(t = 0, r) = 0$ , which is shown here. The decay rate is independent of the circulation  $C$ .

Eq. (19)]. For further discussion of power-law decay in the DBT context, see Sec. IIE in Ref. [19].

## B. Quasinormal modes in the frequency domain

It is well-known that the origin of QN ringing and power law decay may be understood by considering the decomposition of the Green’s function in the frequency domain (see for example [31, 32]). Let us briefly recap the argument here. A formal solution of Eq. (7) with arbitrary initial condition  $\psi_m^0(x) \equiv \psi_m(t = 0, x)$ ,  $\dot{\psi}_m^0(x) \equiv \partial_t \psi_m(t, x)|_{t=0}$  may be written as

$$\psi_m(t, x) = \int \left[ G(x, x', t) \dot{\psi}_m^0(x') + \partial_t G(x, x', t) \psi_m^0(x') \right] dx', \quad (21)$$

where  $x = r_*$ ,  $x' = r'_*$  and  $G$  is the (retarded) Green’s function defined by

$$\left[ \frac{\partial^2}{\partial r_*^2} - \left( \frac{\partial}{\partial t} + \frac{iCm}{r^2} \right)^2 - V_m(r) \right] G = \delta(t) \delta(x - x'), \quad (22)$$

and  $G = 0$  for  $t \leq 0$ . The Green’s function may be written in terms of an inverse Fourier transform

$$G(x, x', t) = \frac{1}{2\pi} \int_{-\infty - ic}^{\infty + ic} \hat{G}(x, x', \omega) e^{-i\omega t} d\omega, \quad (23)$$

with  $c$  positive and real. The frequency-domain function  $\hat{G}$  is constructed in the following way:

$$\hat{G}(x, x', \omega) = -\frac{1}{2i\omega A_{m\omega}^{\text{in}}} \begin{cases} u_{m\omega}^{\text{in}}(x) u_{m\omega}^{\text{up}}(x'), & x \leq x', \\ u_{m\omega}^{\text{in}}(x') u_{m\omega}^{\text{up}}(x), & x \geq x'. \end{cases} \quad (24)$$

Here  $u_{m\omega}^{\text{in}}(r)$  ('in') and  $u_{m\omega}^{\text{up}}(r)$  ('up') are solutions of the homogeneous equation

$$\left[ \frac{d^2}{dr_*^2} + \left( \omega - \frac{Cm}{r^2} \right)^2 - V_m(r) \right] u(r) = 0 \quad (25)$$

that are, respectively, ingoing at the horizon and outgoing at infinity, satisfying the following asymptotic boundary conditions

$$u_{m\omega}^{\text{in}}(r_*) \sim \begin{cases} e^{-i\tilde{\omega}r_*}, & r_* \rightarrow -\infty, \\ A_{m\omega}^{\text{out}} e^{+i\tilde{\omega}r_*} + A_{m\omega}^{\text{in}} e^{-i\tilde{\omega}r_*}, & r_* \rightarrow +\infty, \end{cases} \quad (26)$$

and

$$u_{m\omega}^{\text{up}}(r_*) \sim \begin{cases} B_{m\omega}^{\text{out}} e^{+i\tilde{\omega}r_*} + B_{m\omega}^{\text{in}} e^{-i\tilde{\omega}r_*}, & r_* \rightarrow -\infty, \\ e^{+i\tilde{\omega}r_*}, & r_* \rightarrow +\infty, \end{cases} \quad (27)$$

where  $\tilde{\omega} = \omega - mC/D^2$ .

The frequency-domain Green's function  $\hat{G}$  given in Eq. (24) has poles at frequencies for which  $A_{m\omega}^{\text{in}} = 0$ . Such poles do not lie on the real frequency axis, but rather in the lower half of the complex frequency plane. For  $t > 0$ , the contour of integration in Eq. (23) may be closed in the lower half-plane, as described e.g. in Refs. [31, 32], enclosing the poles. By Cauchy's theorem there arises a sum over residues of these poles, which is known as a 'QN mode sum'. The QN mode sum manifests itself as the damped ringing response seen e.g. in Fig. 1. Furthermore, there exists a branch point in  $\hat{G}$  at zero frequency, which necessitates a branch cut along the negative imaginary axis. The integral of  $\hat{G}$  along either side of the branch cut is associated with the power-law decay at late times, as observed in Fig. 2. With this in mind, let us now consider the QN spectrum, i.e. the set of frequencies defined by  $A_{m\omega}^{\text{in}} = 0$ .

### C. The quasinormal mode spectrum

#### 1. The $m = 0$ mode

The  $m = 0$  mode is isotropic and independent of  $C$ , and furthermore, Eq. (25) has a simple closed-form solution in this case. The 'in' mode is

$$u_{0\omega}^{\text{in}}(r) = r^{1/2} e^{-i\beta} (i\beta)^{i\beta} \Gamma(1 - i\beta) I_{-i\beta}(i\omega r f^{1/2}), \quad (28)$$

where  $\beta \equiv \omega D$  and  $I_\nu(z)$  is a modified Bessel function of the first kind [33]. In this case, the boundary condition constants are

$$A_{0\omega}^{\text{out}} = (2\pi i\beta)^{-1/2} e^{-i\beta} (i\beta)^{i\beta} \Gamma(1 - i\beta), \quad (29)$$

$$A_{0\omega}^{\text{in}} = i e^{\pi\beta} A_{0\omega}^{\text{out}}. \quad (30)$$

The 'up' mode is

$$u_{0\omega}^{\text{up}}(r) = \frac{(2i\pi\omega r)}{2 \sinh(\pi\beta)} \left[ e^{\pi\beta} I_{+i\beta}(i\omega r f^{1/2}) - e^{-\pi\beta} I_{-i\beta}(i\omega r f^{1/2}) \right]. \quad (31)$$

The exact solutions make it clear that there are *no* quasinormal modes for  $m = 0$ . The solutions for higher modes  $m \neq 0$  also have closed form expressions, but in terms of the lesser-known confluent Heun functions (see e.g. [34]).

### 2. Symmetries of the spectrum

Through our time-domain simulations we found that QN ringing is a key feature in the response of higher modes ( $m \neq 0$ ). Although only one QN mode frequency is apparent in the time-domain data of Fig. 1, for each mode  $m \neq 0$  there is in fact an infinite number of damped overtones present in the QN spectrum, labeled by  $n = 0, 1, \dots, \infty$ . For a given  $m, n$ , there is a pair of modes: one co-rotating (+) and one counter-rotating (−) with the circulating flow, with frequencies  $\omega_{mn}^\pm(C)$ . The spectrum has the following symmetries:

$$\omega_{m,n}^\pm(C) = -\omega_{-m,n}^{\pm*}(C) \quad (32)$$

and

$$\omega_{m,n}^\pm(C) = \omega_{-m,n}^\mp(-C), \quad (33)$$

where  $*$  denotes complex-conjugation. Note that (for  $C > 0$ ) the co-rotating mode oscillates and decays faster than the counter-rotating mode, i.e.  $|\text{Re}(\omega_{mn}^+)| \geq |\text{Re}(\omega_{mn}^-)|$  and  $|\text{Im}(\omega_{mn}^+)| \geq |\text{Im}(\omega_{mn}^-)|$  (with equality if  $C = 0$ ), and the frequencies scale linearly with  $1/D$ .

### D. The continued-fraction method

The *continued fraction method* is a fast and accurate numerical method for determining QN frequencies. It was first applied to determine the QN spectrum of black holes in Ref. [35], and was adapted to the draining bathtub case in Ref. [20]. Here we briefly recap the method giving some results in Sec. III G.

The starting point is an ansatz for the QN wavefunction (setting  $D = 1$ ),

$$\psi_{m\omega}(r) = e^{i\omega r} \left( \frac{r-1}{r+1} \right)^{-i\tilde{\omega}/2} \sum_{k=0}^{\infty} a_k (1-r^{-1})^k. \quad (34)$$

It was shown in Ref. [20] that the coefficients  $a_k$  satisfy a four-term recurrence relation, and, by making use of Gaussian elimination, it may be reduced to a three-term relation,

$$\alpha_k a_{k+1} + \beta_k a_k + \gamma_k a_{k-1} = 0. \quad (35)$$

Here  $\alpha_k, \beta_k$  and  $\gamma_k$ , are complex coefficients that depend upon the frequency  $\omega$  and also upon  $m, C$  and  $D$ . For Eq. (34) to represent a valid QN mode solution, the sum  $\sum_k a_k$  must converge to a finite value. This condition is equivalent to the following continued-fraction condition:

$$\beta_0 - \frac{\alpha_0 \gamma_1}{\beta_1 -} \frac{\alpha_1 \gamma_2}{\beta_2 -} \frac{\alpha_2 \gamma_3}{\beta_3 -} \dots = 0. \quad (36)$$

Finding the roots of Eq. (36) in the complex-frequency domain is a straightforward task for a numerical minimization algorithm. High numerical accuracy for the QN frequencies may be obtained.

In the left plot of Fig. 3 we show the dependence of the ‘fundamental’ ( $n = 0$ ) mode on  $m$  and on the rotation rate  $C$  of the acoustic hole. The spectrum exhibits the symmetries (32) and (33). In the non-rotating case ( $C = 0$ ) the two modes  $\omega_{mn}^+$  and  $\omega_{mn}^-$  are symmetric under reflection in the imaginary axis. The introduction of rotation ( $C \neq 0$ ) breaks this symmetry. The co-rotating (+) mode increases the magnitude of its real and imaginary parts, whereas the counter-rotating mode (−) moves in the opposite way. In the limit of very large  $C$ , the imaginary part of the least-damped ( $n = 0$ ) counter-rotating mode asymptotes to zero, whereas the imaginary part of the co-rotating mode increases without bound.

Somewhat different behavior is observed in the spectrum of equatorial modes ( $m = l$ ) of the Kerr black hole (BH), illustrated in the right plot of Fig. 3. In the Kerr case, the relevant rotation parameter is  $a = J/M$  (rather than  $C$ ), where  $J$  and  $M$  are the angular momentum and mass of the BH, respectively. As in the DBT case, the co-rotating (+) modes oscillate more rapidly than the counter-rotating modes (−),  $|\text{Re}(\omega_{lmn}^+)| \geq |\text{Re}(\omega_{lmn}^-)|$ . However, unlike the DBT, the imaginary part of both modes ( $\pm$ ) is found to decrease in magnitude as the rotation rate increases.

### E. Geometric interpretation

This behaviour may be understood through an approximate formula for the QN frequencies [36, 37],

$$\omega_{mn}^\pm \approx \Omega^\pm m - i\Lambda^\pm(n + 1/2). \quad (37)$$

Here,  $\Omega^\pm$  is the orbital frequency of the prograde (+) or retrograde (−) orbit, and  $\Lambda^\pm$  is the corresponding *Lya-punov exponent* [38, 39]. In the case of the DBT, we have

$$\Omega^\pm = 1/l_c^\pm, \quad \Lambda^\pm = 1/r_c^\pm, \quad (38)$$

where  $l_c^\pm$  and  $r_c^\pm$  are given in Eqs. (17) and (16), respectively. Since  $r_c^-$  and  $l_c^-$  increase in magnitude with  $C$ , the magnitude of the real and imaginary parts of  $\omega_{mn}^-$  decreases with  $C$  (and the opposite is true for  $r_c^+$ ,  $l_c^+$  and  $\omega_{mn}^+$ ). By comparison, for the Kerr BH one has instead

$$\Omega^\pm = 1/b_c^\pm, \quad \Lambda^\pm = \frac{1 - 2a/b_c^\pm}{\sqrt{(b_c^\pm)^2 - a^2}}, \quad (39)$$

where

$$r_c^\pm = 2M \left[ 1 + \cos \left( \frac{2}{3} \cos^{-1}(\mp a/M) \right) \right], \quad (40)$$

$$b_c^\pm = \pm 3\sqrt{Mr_c^\pm} - a, \quad (41)$$

for the equatorial orbit [37]. Expanding  $\Lambda^\pm$  gives

$$\Lambda^\pm = (27)^{-1/2} \left[ 1 - \frac{2a^2}{27} \mp \frac{10\sqrt{3}}{243}a^3 + \mathcal{O}(a^4) \right]. \quad (42)$$

Clearly, for both co- and counter-rotating equatorial orbits on Kerr,  $\Lambda^\pm$  decreases with  $|a|$ . This ‘explains’ the observation in the right plot of Fig. 3 that the damping decreases with  $|a|$ .

In Ref. [27], a more accurate approximation for the QN modes of the Kerr BH was found using a ‘geodesic expansion method’, which builds upon the understanding of the properties of the null orbits. Let us now apply this method in the DBT case.

### F. The geodesic expansion method

First let us rewrite the function  $u(r)$  appearing in Eq. (25) using the following ansatz [26, 27]:

$$u_m(r) = \chi(r) \exp \left[ i \int^{r_*} \alpha(r') dr' \right], \quad (43)$$

where

$$\alpha = \left( \omega - \frac{Cm}{r^2} \right) \left( 1 - \frac{Cr_c}{r^2} \right)^{-1} \left( 1 - \frac{r_c^2}{r^2} \right). \quad (44)$$

Note that here  $r_c = r_c^\pm$  and  $l_c = l_c^\pm$ , i.e. representing either the co- or counter-rotating cases, as defined in Eqs. (16) and (17), respectively; we drop the superscript here for simplicity. Substituting ansatz (43) into the radial equation (25) leads to an equation for the function  $\chi(r)$ , namely

$$f\chi'' + (f' + 2i\alpha)\chi' + \left( i\alpha' + \frac{l_c^2 \left( \omega - \frac{Cm}{r^2} \right)^2}{r^2 \left( 1 - \frac{Cl_c}{r^2} \right)^2} - \frac{(m^2 - \frac{1}{4})}{r^2} - \frac{5D}{4r^4} \right) \chi = 0, \quad (45)$$

where  $'$  denotes differentiation with respect to  $r$ . Now, to seek the QN frequencies  $\omega_{mn}$  and radial wave functions  $\chi(r)$  we introduce an expansion in terms of inverse powers of  $m$ , namely

$$l_c \omega_{mn} = \sum_{q=-1}^{\infty} m^{-q} \omega_q^{(n)}, \quad (46)$$

$$\chi = \left[ \xi^n + \sum_{i=0}^n \sum_{j=0}^{\infty} a_{ij}^{(n)} m^{-j} \xi^{n-i} \right] \times \prod_{q=0}^{\infty} \exp \left( m^{-q} S_q^{(n)}(r) \right), \quad (47)$$

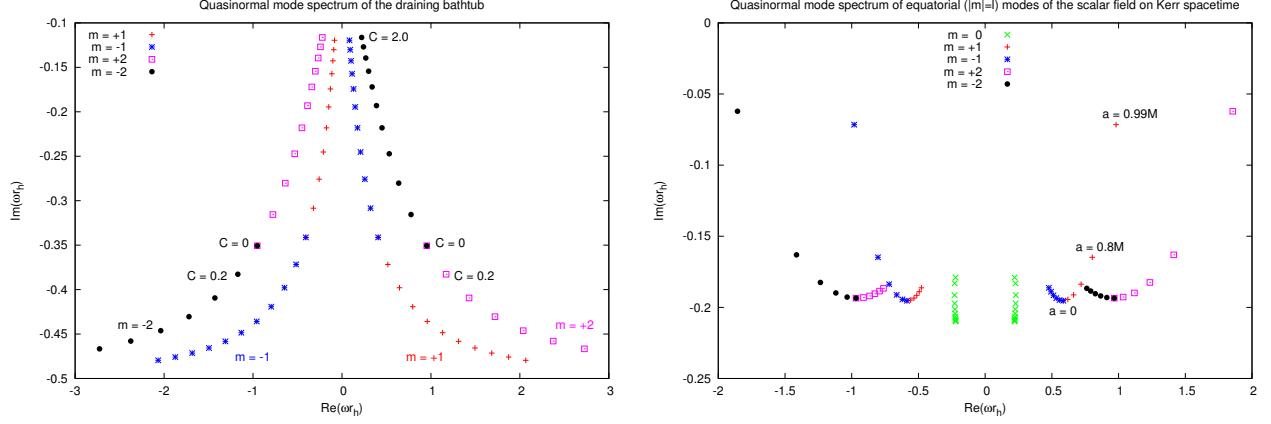


FIG. 3: *Left*: QN mode spectrum of the draining bathtub. *Right*: QN mode spectrum of the equatorial modes of the scalar field on Kerr spacetime. The left plot shows the fundamental ( $n = 0$ ) quasinormal mode frequencies  $\omega_{mn}^{\pm}$  of modes  $m = \pm 1$  and  $\pm 2$ , for a range of circulation rates,  $C = 0, 0.2, 0.4, \dots, 2.0$ . For each mode  $m \neq 0$  there are two QN frequencies  $\omega_m^{\pm}$ . In the non-circulating case ( $C = 0$ ), the spectrum is symmetric. Circulation creates a difference between co-rotating ( $\omega_m^+$ ) and counter-rotating ( $\omega_m^-$ ) modes: Counter-rotating modes oscillate and decay more slowly than co-rotating modes ( $|\text{Re}(\omega_m^+)| > |\text{Re}(\omega_m^-)|$  and  $|\text{Im}(\omega_m^+)| > |\text{Im}(\omega_m^-)|$ ). The spectrum obeys the symmetries of Eqs. (32) and (33). The right plot shows the fundamental ( $n = 0$ ) quasinormal mode frequencies  $2M\omega_{lmn}^{\pm}$  of equatorial ( $|m| = l$ ) modes  $m = 0, \pm 1$  and  $\pm 2$  of the scalar field on the Kerr spacetime, for a range of the black hole rotation rates  $a/M = 0, 0.2, 0.4, 0.6, 0.8, 0.99$ . Co-rotating modes oscillate more rapidly than counter-rotating modes,  $|\text{Re}(\omega_{lmn}^+)| \geq |\text{Re}(\omega_{lmn}^-)|$ . In general, both co- and counter-rotating modes become less damped as the rotation rate increases.

where  $\xi \equiv 1 - r_c^{\pm}/r$ . Here  $\varpi_q^{(n)}$  and  $a_{ij}^{(n)}$  are dimensionless coefficients, and  $S_q^{(n)}(r)$  are smooth radial functions. To determine these unknowns, we impose a condition of regularity upon the solution at  $r = r_c$ .

Let us illustrate the approach by computing the QN frequencies and radial wave functions for the fundamen-

tal mode ( $n = 0$ ) for the co-rotating case. Substituting the expansions in Eqs. (46) and (47) into the radial equation (45), and then rewriting it in terms of the powers of  $m$  associated with coefficients of the expansion, leads to the following system of equations:

$$\mathcal{O}(m^2) : \quad \frac{\left(\varpi_{-1} - \frac{r_c^2 - l_c^2/2}{r^2}\right)^2}{r^2 \left(1 - \frac{(r_c^2 - l_c^2/2)}{r^2}\right)^2} - \frac{1}{r^2} = 0 \quad \Rightarrow \quad \varpi_{-1} = 1, \quad (48)$$

$$\mathcal{O}(m^1) : \quad \frac{2r_c^2(r^2 - [r_c^2 - l_c^2/2])}{l_c r^5} + \frac{2i}{l_c} \left(1 - \frac{[r_c^2 - l_c^2/2]}{r^2}\right) \left(1 - \frac{r_c^2}{r^2}\right) S'_0 + \frac{2\varpi_0 l_c}{r^2} = 0, \quad (49)$$

etc., where the superscript  $n$  has been suppressed for simplicity. Equation (48) is identically satisfied through the choice  $\varpi_{-1} = 1$ . To solve Eq. (49) we impose that  $S_0(r)$  is regular at  $r = r_c$ , which leads to  $\varpi_0 = -il_c/2r_c$  and to the first-order differential equation

$$\frac{dS_0^{(0)}}{dr} = \frac{-2r_c^4 - 2rr_c^3 + l_c^2(r_c^2 + rr_c + r^2)}{[(l_c^2 - 2r_c^2)(r_c + r) + 2r^2r_c + 2r^3]rr_c}. \quad (50)$$

If desired, the radial function  $S_0$  may be obtained by integrating this equation. In subsequent equations at orders  $\mathcal{O}(m^0)$  and higher, the second derivative  $S_0''$  ap-

pears, which may be obtained by differentiating (50). The higher-order equations are solved in a similar way: taking the equation at  $\mathcal{O}(m^{1-k})$  we first impose the continuity condition at  $r = r_c$  to obtain  $\varpi_k$ , and next solve to obtain  $S'_k$ .

Using a symbolic algebra package (e.g. Maple or Mathematica), this procedure may be automated, and the expansion may be taken to higher orders. We have computed the expansion of the QN frequency up to the order  $\mathcal{O}(m^{-9})$ . Below, we quote the expansion of the frequency of a general overtone  $n$  ( $= N - 1/2$ ) up to order  $\mathcal{O}(m^{-4})$ :

$$\begin{aligned}
l_c \omega_{mn} = & m - \frac{l_c}{r_c} N + m^{-1} \left[ \frac{1}{128} \frac{l_c^2}{r_c^4} (5l_c^2 - 16r_c^2) - \frac{3}{32} \frac{l_c^4}{r_c^4} N^2 \right] + m^{-2} i \left[ \frac{1}{4096} l_c^3 (5l_c^4 - 144l_c^2 r_c^2 + 384r_c^4) \frac{1}{r_c^7} N \right. \\
& + \frac{1}{1024} l_c^5 (23l_c^2 - 80r_c^2) \frac{1}{r_c^7} N^3 \left. \right] + m^{-3} \frac{1}{r_c^{10}} \left[ -\frac{1}{1048576} l_c^4 (64640l_c^2 r_c^4 - 21040r_c^2 l_c^4 + 2125l_c^6 - 57344r_c^6) \right. \\
& + \frac{1}{131072} l_c^4 (3456l_c^2 r_c^4 - 976r_c^2 l_c^4 + 75l_c^6 - 4096r_c^6) N^2 + \frac{5}{65536} l_c^6 (896r_c^4 - 592l_c^2 r_c^2 + 91l_c^4) N^4 \left. \right] + \mathcal{O}(m^{-4}).
\end{aligned} \tag{51}$$

Note that, for a given  $m$ , this expression yields two QN frequencies:  $\omega_{mn}^+$  obtained using co-rotating geodesic parameters ( $l_c^+, r_c^+$ ) and  $\omega_{mn}^-$  obtained using counter-rotating geodesic parameters ( $l_c^-, r_c^-$ ). The frequency expansion exhibits the symmetries (32) and (33), as may be confirmed with the aid of the relations  $r_c^\pm(C) = r_c^\mp(-C)$  and  $l_c^\pm(C) = -l_c^\mp(-C)$ .

### G. Validation

In Table I we compare the QN frequencies found via Eq. (51) with numerically-accurate values obtained via the continued-fraction method of Ref. [20]. At large  $m$ , we find excellent agreement. At small  $m$ , the approximation is not so good. For instance, for  $m = 1$  the most accurate estimate was found by truncating the series at  $\mathcal{O}(m^{-3})$ , suggesting that Eq. (51) is in fact an asymptotic series. In Fig. 4 we plot the difference between continued-fraction and geodesic-expansion results, to confirm that Eq. (51) is indeed valid to the stated order in the large- $|m|$  regime.

## IV. REGGE POLE RESONANCES AND THE COMPLEX ANGULAR MOMENTUM METHOD

Regge poles (RPs) are closely related to QN modes [40]. Both types of resonance are associated with the zeros of  $A_{m\omega}^{\text{in}}$ . Whereas QN modes occur at real values of  $m$  (and complex  $\omega$ ), the Regge poles (RPs) occur for real values of  $\omega$  (and complex  $m$ ). That is,  $m_{\omega n}$  is a Regge pole angular momentum if

$$A_{m\omega}^{\text{in}}(\omega, m_{\omega n}) = 0. \tag{52}$$

### A. Methods

Given the close relationship between QN modes and RPs, it is no surprise to find that methods used for QN

modes can be easily adapted to locate RPs [23, 41]. For instance, the continued-fraction method (Sec. III D) may be used without modification, if  $m$  is allowed to become complex. Furthermore, the geodesic expansion method

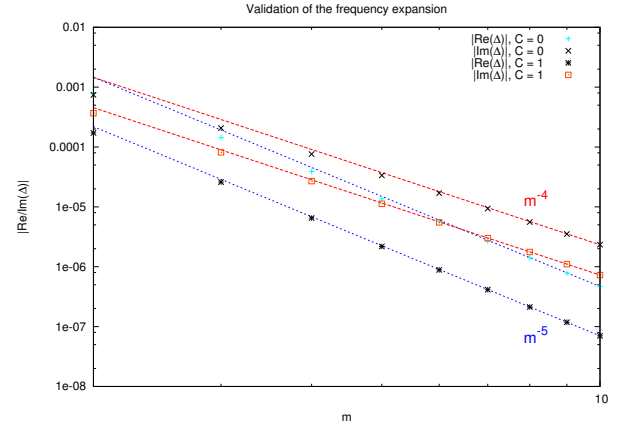


FIG. 4: Validation of the frequency expansion, Eq. (51). The log-scaled plot shows the real and imaginary parts of  $\Delta$  as a function of mode number  $m$ , for the cases  $C = 0$  and  $C = 1$  (and  $D = 1$ ). Here  $\Delta \equiv \omega_{\text{CF}} - \omega_{\text{exp}}$ , where  $\omega_{\text{CF}}$  is the QN frequency obtained via the continued fraction method and  $\omega_{\text{exp}}$  is the frequency estimate given by Eq. (51). The plot shows that the imaginary (real) part of  $\Delta$  scales as  $m^{-4}$  ( $m^{-5}$ ), as predicted by Eq. (51).

(Sec. III F) can be easily modified to find RPs [26]. Either one may repeat the arguments of Sec. III F, or one may take the following simple steps: (i) assume that the Regge poles have the expansion of the form

$$m_{\omega n} = \zeta_{-1}\omega + \zeta_0 + \zeta_1\omega^{-1} + \dots, \tag{53}$$

(ii) substitute the expansion for QN frequencies into the above equation, and (iii) solve order-by-order in  $m$  to find the expansion coefficients  $\zeta_k$ . We find



TABLE I: QN frequencies of the fundamental mode ( $n = 0$ ) for  $m = 1 \dots 5$ . The second column gives the frequencies determined via the continued-fraction method of Sec. III D. The third column gives the frequencies estimates from the expansion method, Eq. (51). The numeral in parentheses indicates the absolute error in the last displayed digit, where the error in the expansion method was estimated from the magnitude of the final terms in the series, Eq. (51).

$D = 1, C = 0$ , symmetric modes ( $\pm$ )		
$m$	Continued-Fraction	Expansion Method
1	$\pm 0.4068326196672(2) - 0.341236118125(2)i$	$\pm 0.40(1)^* - 0.345(8)i^*$
2	$\pm 0.95272808772474(6) - 0.3507394957317(2)i$	$\pm 0.9524(9) - 0.3511(2)i$
3	$\pm 1.46854069662523(5) - 0.3524255329360(2)i$	$\pm 1.46854(6) - 0.352444(8)i$
4	$\pm 1.9764527143560(1) - 0.3529594212624(2)i$	$\pm 1.976453(8) - 0.352961(1)i$
5	$\pm 2.4811874975616(1) - 0.35318833783278(6)i$	$\pm 2.481188(2) - 0.3531886(1)i$
$D = 1, C = 1$ , counter-rotating modes ( $-$ )		
$m$	Continued-Fraction	Expansion Method
1	$-0.1490148506555(1) - 0.1945123420127(2)i$	$-0.14(1) - 0.200(8)i$
2	$-0.3875750711220(2) - 0.1930307208974(1)i$	$-0.38753(6) - 0.19296(9)i$
3	$-0.6040167016214(2) - 0.19220554998274(1)i$	$-0.604014(4) - 0.192204(3)i$
4	$-0.8155812868761(1) - 0.1918516723182(3)i$	$-0.8155811(5) - 0.1918515(3)i$
5	$-1.0253078467593(1) - 0.1916753960108(2)i$	$-1.0253078(1) - 0.19167538(6)i$
$D = 1, C = 1$ , co-rotating modes ( $+$ )		
$m$	Continued-Fraction	Expansion Method
1	$+1.13097639081141(2) - 0.4485344193663(3)i$	$+1.134(9) - 0.445(7)i$
2	$+2.3742286767072(2) - 0.45797306346650(6)i$	$+2.37421(3) - 0.45791(2)i$
3	$+3.5943282234311(3) - 0.4600949990202(3)i$	$+3.594327(2) - 0.460093(2)i$
4	$+4.8080846946733(2) - 0.46088327915183(4)i$	$+4.8080845(3) - 0.4608831(2)i$
5	$+6.0192217565670(3) - 0.4612576561145(2)i$	$+6.01922173(6) - 0.46125763(3)i$

$$\begin{aligned}
m_{\omega n} = & l_c \omega + \frac{il_c}{r_c} N + \left[ \frac{3l_c^3 N^2}{32r_c^4} + \frac{l_c (16r_c^2 - 5l_c^2)}{128r_c^4} \right] \omega^{-1} - iN \left[ \frac{l_c}{4096r_c^7} (-304r_c^2 l_c^2 + 5l_c^4 + 896r_c^4) \right. \\
& + \frac{l_c^3}{1024r_c^7} (16r_c^2 + 23l_c^2) N^2 \left. \right] \omega^{-2} + \left[ \frac{l_c (-73728r_c^6 + 74880r_c^4 l_c^2 - 22640r_c^2 l_c^4 + 2125l_c^6)}{1048576r_c^{10}} \right. \\
& - \frac{l_c (36864r_c^6 - 7808r_c^4 l_c^2 - 1616r_c^2 l_c^4 + 75l_c^6)}{131072r_c^{10}} N^2 - \frac{l_c^3 (384r_c^4 + 560r_c^2 l_c^2 + 455l_c^4)}{65536r_c^{10}} N^4 \left. \right] \omega^{-3} + \mathcal{O}(\omega^{-4}), \quad (54)
\end{aligned}$$

where  $N = n + 1/2$ . Again, as for Eq. (51), we note that this expression yields two separate values,  $m_{\omega n}^{\pm}$ , obtained by using either co-rotating or counter-rotating geodesic parameters ( $l_c^{\pm}, r_c^{\pm}$ ). We also note that it is straightforward to take the expansion to much higher orders.

### B. Spectrum

The Regge pole spectrum has the following symmetries

$$m_{\omega, n}^{\pm}(C) = -m_{\omega, n}^{\pm*}(C) \quad (55)$$

and

$$m_{\omega, n}^{\pm}(C) = -m_{\omega, n}^{\mp}(-C). \quad (56)$$

The Regge pole spectrum in the complex- $m$  plane is illustrated in Fig. 5. For  $\omega > 0$ , the co-rotating (+) modes lie in the first quadrant, and the counter-rotating (-) modes lie in the fourth quadrant. In the non-rotating case, the spectrum is symmetric,  $m_{\omega n}^+ = -m_{\omega n}^-$ . For  $C > 0$ , the real and imaginary parts of  $m_{\omega n}^+$  decrease with  $C$ , whereas the real and imaginary parts of  $-m_{\omega n}^-$  increase with  $C$ , as expected from Eq. (54).

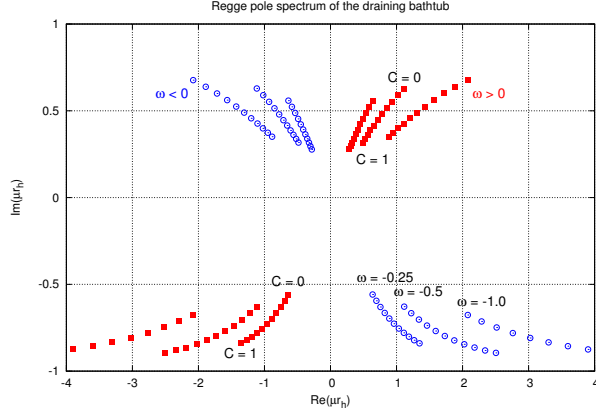


FIG. 5: Regge pole spectrum of the draining bathtub. For three frequencies  $|\omega| = 0.25, 0.5$ , and  $1.0$ , we plot points for rotation rates  $C/r_h = 0, 0.1, 0.2, \dots, 1$ , showing the fundamental ( $n = 0$ ) Regge pole values  $m_{\omega n}r_h$  in the complex- $m$  plane. Co-rotating and counter-rotating modes are shown; they exhibit the symmetries (55) and (56). For  $C > 0$ , the co-rotating (counter-rotating) modes lie in the upper (lower) half plane.

### C. Absorption Cross Section and Regge Poles

The absorption cross section  $\sigma$  of the draining bathtub was studied in Ref. [28]. It may be obtained from a sum over partial wave contributions, via

$$\sigma = \frac{1}{\omega} \sum_{m=-\infty}^{\infty} \left( 1 - \left| \frac{A_{m\omega}^{\text{out}}}{A_{m\omega}^{\text{in}}} \right|^2 \right). \quad (57)$$

At high frequencies, the absorption cross section is seen to approach the ‘geometric’ capture cross section,  $\sigma_{\text{geo}} = |b_c^+| + |b_c^-| = 4\sqrt{D^2 + C^2}$ . In the non-rotating case,  $C = 0$ ,  $\sigma$  displays regular damped oscillations with increasing frequency. With increasing  $C$ , these oscillations become less regular (cf. Fig. 6).

Recent papers by Decanini, Folacci and collaborators [24, 25] on the universality of high-frequency absorption cross sections for *spherically-symmetric* black holes use complex angular momentum (CAM) methods [21, 22, 40, 42] to show how oscillations in the cross section as a function of wave frequency  $\omega$  are directly related to the Regge pole spectrum. In this section, we extend the calculation to treat a *rotating* system, for the first time.

To apply CAM methods, we must be able to analytically continue  $\sigma$  into the complex- $m$  plane. Let us therefore define

$$\sigma = \frac{1}{\omega} \sum_{m=-\infty}^{\infty} \Gamma(m), \quad (58)$$

where

$$\Gamma(m) = 1 - \frac{A_{m\omega}^{\text{out}}(A_{m^*\omega}^{\text{out}})^*}{A_{m\omega}^{\text{in}}(A_{m^*\omega}^{\text{in}})^*}. \quad (59)$$

A sum like the one above can be expressed as a contour integral using the Watson transformation, i.e.

$$\sigma = \frac{i}{2\omega} \int_{\mathcal{C}} \frac{e^{i\pi m}}{\sin(\pi m)} \Gamma(m) dm, \quad (60)$$

where now  $m$  takes complex values. Here the contour of integration  $\mathcal{C}$  encloses in a clockwise sense all (and only) the poles of the integrand that lie on integer values on the real axis at  $m = -\infty, \dots, +\infty$ , i.e.

$$\int_{\mathcal{C}} = \int_{\mathcal{C}_+} - \int_{\mathcal{C}_-}, \quad \text{where} \quad \int_{\mathcal{C}_{\pm}} = \int_{-\infty \pm ic}^{\infty \pm ic}, \quad (61)$$

for some small positive real value  $c$ . Next, we use the identity  $e^{i\pi m} = e^{-i\pi m} + 2i \sin(\pi m)$  to obtain

$$\begin{aligned} \sigma &= \sigma_{\text{int}} + \frac{i}{2\omega} \int_{\mathcal{C}_+} \frac{e^{i\pi m} \Gamma(m)}{\sin(\pi m)} dm \\ &\quad - \frac{i}{2\omega} \int_{\mathcal{C}_-} \frac{e^{-i\pi m} \Gamma(m)}{\sin(\pi m)} dm, \end{aligned} \quad (62)$$

where

$$\sigma_{\text{int}} = \frac{1}{\omega} \int_{-\infty}^{\infty} \Gamma(m) dm. \quad (63)$$

The contour  $\mathcal{C}_+$  may be closed in the upper half-plane, enclosing poles of  $\Gamma(m)$  at  $m_{\omega n}^+$  and  $m_{\omega n}^{*-}$ . Likewise, the contour  $\mathcal{C}_-$  may be closed in the lower half-plane, enclosing the poles of  $\Gamma(m)$  at  $m_{\omega n}^-$  and  $m_{\omega n}^{+*}$ . This leads to a sum of residues, that is,

$$\sigma = \sigma_{\text{int}} - 2\pi \text{Re} \sum_{\pm} \sum_{n=0}^{\infty} \frac{e^{\pm i\pi m_{\omega n}^{\pm}}}{\sin(\pi m_{\omega n}^{\pm})} \gamma_{\omega n}^{\pm}. \quad (64)$$

Here  $\gamma_{\omega n}^{\pm}$  denotes the residue,

$$\gamma_{\omega n}^{\pm} = \text{Res}_{m \rightarrow m_{\omega n}^{\pm}} [\Gamma(m)], \quad (65)$$

and we have made use of the symmetry relation

$$\text{Res}_{m \rightarrow m_{\omega n}^{\pm}} [\Gamma(m)] = (\gamma_{\omega n}^{\pm})^*. \quad (66)$$

Equation (64) is an exact expression which may be computed numerically. The sum over overtones converges rapidly, due to the damping effect of the imaginary part of the Regge pole. The residues are straightforward to compute, using

$$\gamma_{\omega n}^{\pm} = - \left( \frac{A_{m\omega}^{\text{out}}(A_{m^*\omega}^{\text{out}})^*}{\alpha_{\omega n}^{\pm}(A_{m^*\omega}^{\text{in}})^*} \right)_{m=m_{\omega n}^{\pm}}, \quad (67)$$

where  $A_{m\omega}^{\text{in}} \approx \alpha_{\omega n}^{\pm}(m - m_{\omega n}^{\pm}) + \dots$  in the vicinity of a Regge pole. The integral over frequency can also be performed in a straightforward manner. Numerical results are shown in Fig. 6. We find a very good agreement with the results of the partial wave method of Ref. [28].

To better understand the geometric meaning of Eq. (64) in the high-frequency limit, we may proceed by making some very simplistic approximations:

$$\Gamma(m) \approx \Theta(m - l_c^+ \omega) \Theta(m - l_c^- \omega), \quad (68)$$

and

$$m_{\omega, n=0}^\pm \approx l_c^\pm \omega + \frac{il_c^\pm}{2r_c} + \mathcal{O}(\omega^{-1}), \quad (69)$$

and furthermore

$$\gamma_{\omega n}^\pm \approx -\frac{\eta^\pm}{2\pi} + \mathcal{O}(\omega^{-1}), \quad (70)$$

where  $\eta^\pm = |l_c^\pm / r_c^\pm|$ . Neglecting the higher overtones leads to the simple approximation

$$\sigma_\pm = |l_c^\pm| \left[ 1 + 4\pi\eta^\pm e^{-\pi\eta^\pm} \text{sinc}(2\pi|l_c^\pm|\omega) \right], \quad (71)$$

where  $\sigma = \sigma_+ + \sigma_-$  and  $\text{sinc}(x) = \sin(x)/x$ . Equation (71) makes it clear that the cross section approaches the geometric capture cross section in the high-frequency limit. Furthermore, the cross section exhibits damped oscillations with increasing frequency, which are due to the Regge pole contribution, which are controlled by the geometric quantities ( $l_c^\pm$  and  $r_c^\pm$ ).

In Fig. 6 we compare the results of the partial-wave calculation of Ref. [28] with a numerical calculation based on the exact Regge pole expression, Eq. (64), and the ‘geometric’ high-frequency approximation, Eq. (71). It is clear from the right plot that the co-rotating (counter-rotating) orbits are responsible for oscillations in the profile with a higher (lower) frequency and smaller (larger) amplitude. The superposition of co- and counter-rotating effects creates a rather irregular profile, in contrast with the more regular profile exhibited in the non-rotating case (left plot).

## V. FINAL REMARKS

In this paper we focused our attention on the quasinormal frequencies and Regge poles of the draining bathtub, a simple system which may be studied in the lab and which has been suggested as a simple (though inexact) analogue for the Kerr spacetime [16]. Our aim was to bring together a variety of techniques, both old [20] and new [26, 27, 41], to build up a unified picture of the resonances of a simple non-spherically-symmetric system, for the first time.

We studied the QN resonances numerically in both the time domain (Sec. III A) and the frequency domain (Sec. III B). For the former we developed a purpose-built finite-difference code, and for the latter we applied the continued-fraction method (developed in Ref. [20]). We provided a clear geometric interpretation (Sec. III E) for our numerical results, in terms of the properties of the co-

and counter-rotating photon/phonon orbits of the spacetime (Sec. II B). The geometric interpretation neatly explains the similarities and differences between the DBT and rotating black hole QN spectra (see Fig. 3). Furthermore, the geometric interpretation may be leveraged to obtain an expansion of QN frequencies in inverse powers of  $m$ , as we showed in Sec. III F.

In Sec. IV, we demonstrated how methods developed to investigate QN modes may be simply adapted to investigate the Regge poles (see also e.g. [41]). In the complex angular momentum approach, Regge poles may be used to effectively ‘explain’ the diffraction effects seen in scattering and absorption cross sections [42]. For example, in the context of the Schwarzschild black hole, Regge poles have been implicated in the glory and spiral-scattering oscillations in the scattering cross section  $d\sigma/d\Omega$  at large angles [21, 22], and also in the fine-structure oscillations in the absorption cross section  $\sigma$  [24, 25]. Here, in Sec. IV C, we extended the latter analysis to treat a non-spherically symmetric spacetime for the first time. We showed (Fig. 6) that the superposition of diffraction effects linked to the properties of co- and counter-rotating orbits creates a rather irregular fine-structure [25] in  $\sigma(\omega)$  when the system is rotating.

Let us briefly highlight some analytic results from this study: (i) at late times, perturbations of the DBT undergo power-law decay with an index  $\eta$  given by Eq. (20); (ii) the isotropic ( $m = 0$ ) mode possesses a simple analytic solution, Eq. (28) and (31); (iii) asymptotic expansions for QN and RP frequencies in terms of geometric quantities are given by Eq. (51) and (54), and they are good approximations in the large- $|m|$  regime (Fig. 4); (iv) the absorption cross section may be expressed in terms of Regge poles via Eq. (64); (v) at large frequencies, the simple ‘geometric’ formula Eq. (71) provides a good approximation to  $\sigma$  (see Fig. 6).

In conclusion, we have illustrated how a simple analogue system (the DBT) possesses a spectrum of resonances which, in addition to being of interest in their own right, may improve our understanding of the resonances of a rotating black hole. Whereas black holes are remote celestial entities, analogues may be investigated in the lab today [15]. We hope that an experimental investigation of the resonances of the DBT will be undertaken. The key message from this work is that the presence of distinct co- and counter-rotating photon/phonon orbits in the (effective) spacetime leaves a clear imprint on the resonance spectrum. The superposition of co- and counter-rotating resonances leads to a host of (potentially-observable) effects, for example in QN ringing; in the fine-structure of the absorption cross section; and in diffraction effects in scattered waves. We hope to undertake a study of the latter effects in the near future.

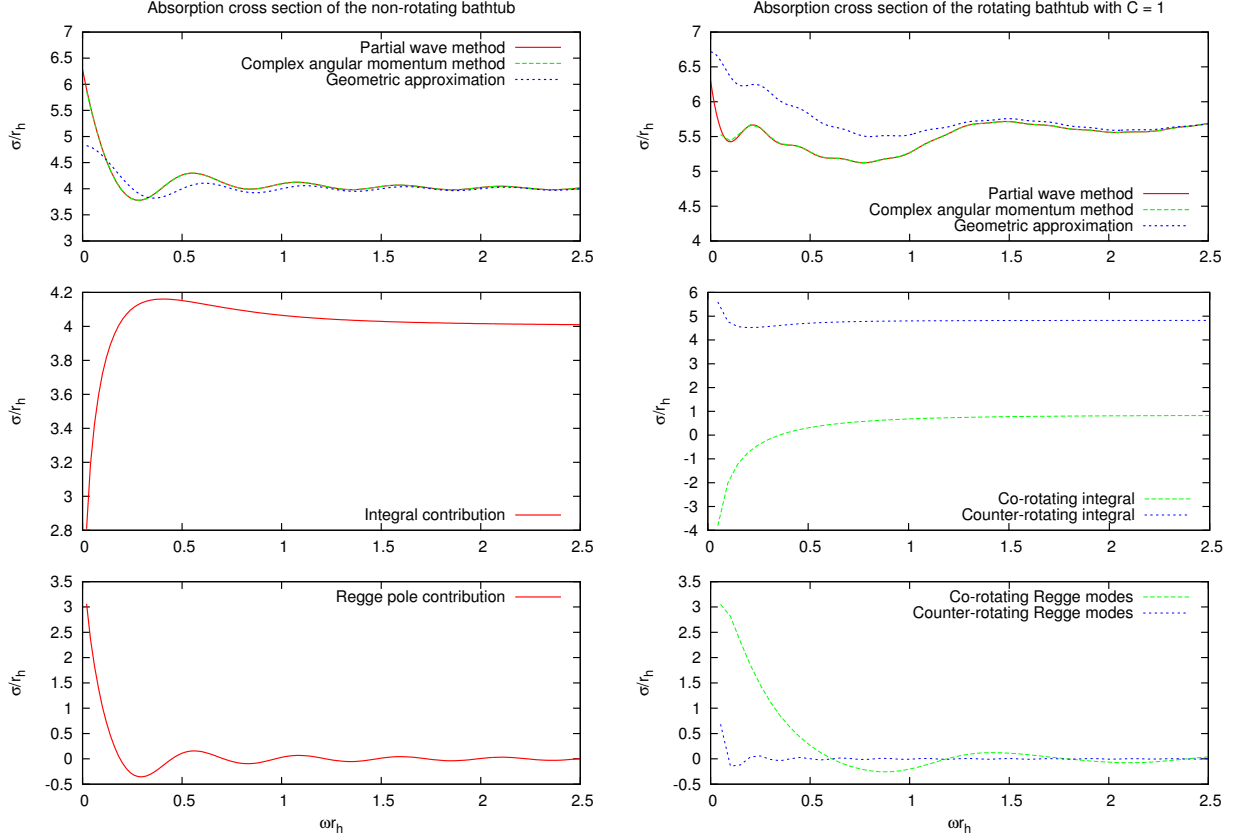


FIG. 6: Absorption cross section as a function of the frequency, for  $C = 0$  and  $C = 1$ . In the upper plots, the solid line shows the absorption cross section  $\sigma$  computed from the partial wave sum [28], the dashed line shows  $\sigma$  computed numerically from the complex angular momentum expression [Eq. (64)], and the dotted line shows the simple geometric approximation [Eq. (71)]. The lower plots show the separate contributions from Regge pole sums and the co-rotating and counter-rotating integrals [Eq. (63)].

### Acknowledgments

The authors would like to thank Conselho Nacional de Desenvolvimento Científico e Tecnológico (CNPq) and Fundação de Amparo à Pesquisa do Estado do Pará (FAPESPA) for partial financial support. S. D. thanks the Universidade Federal do Pará (UFPA) in Belém for

kind hospitality, and acknowledges financial support from the Engineering and Physical Sciences Research Council (EPSRC) under grant no. EP/G049092/1. L. C. and L. O. would like to acknowledge also partial financial support from Coordenação de Aperfeiçoamento de Pessoal de Nível Superior (CAPES).

- 
- [1] K. D. Kokkotas and B. G. Schmidt, *Liv. Rev. Relat.* **2**, 2 (1999).
  - [2] H.-P. Nollert, *Classical Quantum Gravity* **16**, R159 (1999).
  - [3] V. Ferrari and L. Gualtieri, *Gen. Rel. Grav.* **40**, 1572 (2008) [arXiv:0709.0657].
  - [4] E. Berti, V. Cardoso, and A. O. Starinets, *Classical Quantum Gravity* **26**, 163001 (2009) [arXiv:0905.2975].
  - [5] J. Bardeen, B. Carter, and S. Hawking, *Commun. Math. Phys.* **31**, 161 (1973).
  - [6] Y. Décanini and A. Folacci, *Phys. Rev. D* **81**, 024031 (2010) [arXiv:0906.2601].
  - [7] M. Visser, *Classical Quantum Gravity* **15**, 1767 (1998) [arXiv:gr-qc/9712010].
  - [8] W. G. Unruh, *Phys. Rev. Lett.* **46**, 1351 (1981).
  - [9] *Artificial black holes*, edited by M. Novello, M. Visser, and G. Volovik (World Scientific, Singapore, 2002).
  - [10] L. J. Garay, *Int. J. Theor. Phys.* **41**, 2073 (2002).
  - [11] L. J. Garay, J. R. Anglin, J. I. Cirac, and P. Zoller, *Phys. Rev. A* **63**, 023611 (2001).
  - [12] R. Schützhold and W. G. Unruh, *Phys. Rev. Lett.* **95**, 031301 (2005) [arXiv:quant-ph/0408145].
  - [13] F. Belgiorno, S. L. Cacciatori, M. Clerici, V. Gorini, G. Ortenzi, L. Rizzi, E. Rubino, V. G. Sala, and D. Faccio,

- Phys. Rev. Lett. **105**, 203901 (2010).
- [14] S. Giovanazzi, Phys. Rev. Lett. **106**, 011302 (2011).
  - [15] S. Weinfurter, E. W. Tedford, M. C. J. Penrice, W. G. Unruh, and G. A. Lawrence, Phys. Rev. Lett. **106**, 021302 (2011).
  - [16] R. Schützhold and W. G. Unruh, Phys. Rev. D **66**, 044019 (2002).
  - [17] Elsewhere in the literature,  $C$  and  $D$  are alternately referred to as  $B$  and  $A$ , respectively.
  - [18] B. C. Xanthopoulos, Phys. Lett. B **178**, 163 (1986).
  - [19] E. Berti, V. Cardoso, and J. P. S. Lemos, Phys. Rev. D **70**, 124006 (2004) [arXiv:gr-qc/0408099].
  - [20] V. Cardoso, J. P. S. Lemos, and S. Yoshida, Phys. Rev. D **70**, 124032 (2004) [arXiv:gr-qc/0410107].
  - [21] N. Andersson and K.-E. Thylwe, Classical Quantum Gravity **11**, 2991 (1994).
  - [22] N. Andersson, Classical Quantum Gravity **11**, 3003 (1994).
  - [23] Y. Décanini, A. Folacci, and B. Jensen, Phys. Rev. D **67**, 124017 (2003) [arXiv:gr-qc/0212093].
  - [24] Y. Décanini, G. Esposito-Farèse, and A. Folacci, Phys. Rev. D **83**, 044032 (2011) [arXiv:1101.0781].
  - [25] Y. Décanini, A. Folacci and B. Raffaelli, (2011) [arXiv:1104.3285].
  - [26] S. R. Dolan and A. C. Ottewill, Classical Quantum Gravity **26**, 225003 (2009) [arXiv:0908.0329].
  - [27] S. R. Dolan, Phys. Rev. D **82**, 104003 (2010) [arXiv:1007.5097].
  - [28] E. S. Oliveira, S. R. Dolan, and L. C. B. Crispino, Phys. Rev. D **81**, 124013 (2010).
  - [29] W. E. Schiesser, *The Numerical Method of Lines: Integration of Partial Differential Equations* (Academic Press, New York, 1991).
  - [30] O. Rinne, Ph.D. thesis, University of Cambridge (2006) [arXiv:gr-qc/0601064].
  - [31] E. W. Leaver, Phys. Rev. D **34**, 384 (1986).
  - [32] N. Andersson, Phys. Rev. D **55**, 468 (1997).
  - [33] I. S. Gradshteyn and I. M. Ryzhik, *Table of Integrals, Series, and Products* (Academic Press, San Diego, 2000).
  - [34] P. Fiziev, Classical Quantum Gravity **27**, 135001 (2010).
  - [35] E. W. Leaver, Proc. R. Soc. A **402**, 285 (1985).
  - [36] C. J. Goebel, Astrophys. J. **172**, L95 (1972).
  - [37] B. Mashhoon, Phys. Rev. D **31**, 290 (1985).
  - [38] V. Cardoso, A. S. Miranda, E. Berti, H. Witek, and V. T. Zanchin, Phys. Rev. D **79**, 064016 (2009) [arXiv:0812.1806].
  - [39] N. J. Cornish and J. J. Levin, Classical Quantum Gravity **20**, 1649 (2003) [arXiv:gr-qc/0304056].
  - [40] R. G. Newton, *Scattering Theory of Waves and Particles* (Springer, New York, 1982), 2nd ed.
  - [41] Y. Décanini, A. Folacci, and B. Raffaelli, Phys. Rev. D **81**, 104039 (2010).
  - [42] H. M. Nussenzveig, *Diffraction effects in semiclassical scattering* (Cambridge University Press, 1992).